Applied Nanoscience (2023) 13:453–464
https://doi.org/10.1007/s13204-021-01791-x

ORIGINAL ARTICLE

Two-phase modelling of the effects of pore-throat geometry on enhanced oil recovery

Ashi Chauhan[1,2] · Fatemeh Salehi[2] · Salman Jalalifar[2] · Simon M. Clark[1,2]

Received: 21 December 2020 / Accepted: 8 March 2021 / Published online: 1 April 2021

Abstract

This study presents computational fluid dynamics (CFD) analysis of the effects of wettability, viscosity and interfacial tension (IFT) for enhanced oil recovery (EOR) with varying pore configuration. A more realistic pore-throat geometry is studied which was motivated by oil-containing rock configuration that indicates the importance of pore geometry in EOR. The results are compared with those obtained for a simple geometry. Both saturated and unsaturated conditions are considered while the IFT varies. For both geometries, the saturated condition presents 99% of oil recovery, for the water-wet and intermediate states while it is about 88% for the oil-wet state. However, there is a significant difference in the temporal evolution of the oil recovery factor, as the complex model is 1.4 to 3 times slower than the simplified one to achieve maximum oil recovery factor under the same conditions. For unsaturated conditions, two different initial oil volumes were considered to explore the combined effect of low IFT and change in wettability. Similarly, the oil recovery process is significantly slower for the complex geometric configuration. The study of very low IFT values (10, 35, 65 and 75 μN/m) for the complex configuration in the unsaturated oil condition revealed that highest oil recovery is achieved at the IFT of 75 μN/m. The results confirm that geometric configuration plays an important role in EOR. The impact of pore structure becomes more significant in the unsaturated oil state demonstrating that very low values of IFT slow the oil recovery process.

Keywords Wettability · Contact angle · Interfacial tension (IFT) · Nanofluid · Volume of fluid (VOF)

Introduction

Although there are many large oil deposits in the world, most are in the final stages of their lives after the extraction of many billions of barrels of oil every year. Hence, more efficient techniques of oil recovery, such as enhanced oil recovery (EOR) methods, have been in development for the last few decades. EOR methods improve the mobility of oil by reducing viscosity by injection of gas or solvent flooding, chemical flooding, thermal recovery, and combinations of these techniques. Developing environmentally friendly and economical EOR methods is a challenge. Among the various approaches, nanotechnology (Zhao and Wen 2017; Khalili Nezhad and Cheraghian 2016; Hendraningrat and Zhang 2015; Hashemi et al. 2016) and Hendraningrat and Torsæter (2015) has proved to be very successful. Nanoparticles in the water (nanofluid) can change the properties of the dormant fluid (oil) making it more extractable. These properties are surface-to-volume ratio, interfacial tension (IFT), wettability control, thermal conductivity and specific heat, which contribute in the recovery of trapped oil.

The contact angle also plays an important parameter in EOR since it is directly related to wettability. The variations in the contact angle for different nanofluids are summarised in Table 1. It can be seen that for different nanofluids the contact angle ranges from 0° to 134° while for brine it is between 0° and 100° in the presence of other chemicals. The variation of nanoparticle type and their concentration significantly affects the contact angle and consequently, the ORF.

To understand the effect of nanoparticles on oil recovery, pore-scale models were studied by various researchers. Sefiane et al. (2008) experimentally investigated the behaviour of the nanoparticles in wetting and de-wetting solids. The degree of static wetting was defined by θ_e. It was found that when θ_e is larger than 90°, the wetting is not effective, and

✉ Fatemeh Salehi
fatemeh.salehi@mq.edu.au

[1] Department of Earth and Environmental Sciences, Macquarie University, Sydney, Australia

[2] School of Engineering, Macquarie University, Sydney, Australia

Table 1 Contact angles of nanofluids

Material	Type	Contact angle	Refs
Nanofluid (water + nanoparticles)	Aluminium Al_2O_3	60–65	Sefiane et al. (2008)
		41–64	Vafaei et al. (2011)
		0–90	Kim et al. (2006)
		37–60	Chinnam et al. (2015)
		100–131	Joonaki and Ghanaatian (2014)
	TiO_2–DI	33.7–45.1	Radiom et al. (2009)
		27–60	Chinnam et al. (2015)
	Bismuth Telluride	30–60	Vafaei et al. (2011)
	Zirconia	0–90	Kim et al. (2006)
	Silica	0–90	Kim et al. (2006)
		34–59	Chinnam et al. (2015)
		32–134	Joonaki and Ghanaatian (2014)
	ZnO	29–53	Chinnam et al. 2015)
	Fe_2O_3	90–132.5	Joonaki and Ghanaatian (2014)
Brine	Brine + CO_2 + Quartz	20–80	Iglauer et al. (2012)
	Brine + CO_2	35–80	Arif et al. (2016)
	Brine + CO_2 + Mica	0–100	Arif et al. (2016)
	Brine + CO_2	10–45	Saraji et al. (2014)

the liquid was said to be non-wetting while when θ_e smaller than 90°, the liquid wet the solid. As the equilibrium contact angle decreased, the degree of wetting improved until the limiting case of $\theta_e = 0$ was achieved, resulting in complete wetting. Kim et al. (2006) investigated the boiling effects of nanofluids containing alumina nanoparticles. They showed that enhancement in wettability is due to the combined effects of adhesion tension and an increase in surface tension which resulted in a significant reduction in contact angle. It was also found that aluminium and zinc oxides were better for EOR, while silicon dioxide tends to change wettability more in addition to IFT reduction in the reservoir (Joonaki and Ghanaatian 2014).

A further study by Chinnam et al. (2015) showed that contact angle also depends on temperature, volumetric concentration and size of nanoparticles. Radiom et al. (2009) experimentally explored the characterisation of surface tension, and contact angle of a nanofluid. This investigation showed that the surface tension of titanium oxide (TiO_2) with deionised (DI) water was weak and slightly depended on nanoparticle concentration. It also confirmed that there was a smaller surface tension for higher nanoparticle concentrations. The studies of contact angle for brine mixtures showed that the contact angle ranges between 0° and 100° for brine in the presence of CO_2, mica and quartz (Arif et al. 2016; Saraji et al. 2014; Iglauer et al. 2012).

Computational fluid dynamics (CFD) simulations are reliable methods that have been used to study the effect of IFT, wettability, contact angles and fluid velocity on EOR in the presence of nanofluid. The pore-scale numerical and experimental studies of Kondiparty et al. (2011) and Wasan and Nikolov (2003) confirmed that wetting properties of the fluid changed with the injection of nanoparticles while a disjoining pressure gradient enhances the distribution of the wetting film, resulting in the separation of oil particles from the solid surface. Liu et al. (2011) found that the shape of the nanofluids/oil interface strongly depends on local volume concentration. Their research was taken forward by Zhao and Wen (2017) who computationally investigated the oil/water flow characteristics during the pore flooding process. Their results showed that the water-wet state in oil-saturated pores could increase recovery from 25 to 40% compared to the oil-wet state; however, for the unsaturated oil condition, oil recovery was improved by reducing IFT.

The CFD study by Nandwani et al. (2019) showed that a mixture of surfactants showed higher productivity in recovering oil due to negligible fingering effects, extremely lower IFT between the surfactant solution and oil and low diffusion rates of surfactant species into the residual oil. A further CFD study on pore configuration and its distribution in the 2D model showed an increase in the EOR factor with the injection of a nanofluid as it reduced the fingering effect in the porous media and fluid flow in the random pore model (Gharibshahi et al. 2015). Injection of bio-surfactant fluid also accelerated breakthrough time and decreased surface tension between the injected fluid and the oil (Jafari et al. 2017).

Despite these previous studies, it is still not clear how the geometric structure of a pore affects oil recovery. Previous studies considered a single pore structure with a single inlet and outlet (Lv and Wang 2015; Zhao and Wen 2017). This simple configuration may not necessarily represent the main

features of a more realistic, complex pore structure with multiple outlets (Gharibshahi et al. 2015; Jafari et al. 2017). While there are some studies on oil recovery in rocks (Santiago et al. 2016), there are no systematic studies on how the complexity of the pore structure affects the oil recovery. The main objective of this study is to conduct a systematic CFD analysis on the effects of the geometric structure of a pore. This study, for the first time, presents a comparative study on the impact of wettability and IFT on water/oil flow interactions at both saturated and unsaturated conditions as the pore geometry varies. For this purpose, two pore-throat configurations are considered while the complexity of the geometry systematically increases. Our results will enable a more optimised use of agents, such as nanofluids, to enhance oil-recovery in real oil wells.

Methodology

Computational fluid dynamics simulations were carried out to predict fluid flow through pore geometries. For the cases considered in this study, the inlet Reynolds numbers computed using the inlet velocity and the channel size is 0.025 which is much smaller than the critical Reynolds number, confirming the flow is laminar for all cases. Hence, the governing equations for laminar two-phase flows are presented in this section.

Governing equations

The Eulerian–Eulerian volume of fluid (VOF) method is used here. It can model two or more immiscible fluids by solving a single set of momentum equations and tracking the volume fraction of each fluid within a domain. The variables and properties are either purely representative of one of the phases, or representative of a mixture of the phases, depending on the volume fraction values. Hence, if the "qth" fluid's volume fraction in the cell is denoted as α_q, then the following three conditions are possible:

- If $\alpha_q = 0$, then the cell does not contain the qth fluid.
- If $\alpha_q = 1$, then the cell only contains the qth fluid and
- If $0 < \alpha_q < 1$, then the cell contains the interface between the qth fluid and one or more fluids.

Based on the local value of α_q, the properties and variables are calculated. The VOF model is used to obtain the solution of the incompressible Navier–Stokes equations for two-phase flow of oil and water. Conservation of mass and momentum are expressed as:

$$\nabla.\left(\vec{\vartheta}\right) = 0 \tag{1}$$

$$\frac{\partial}{\partial t}(\rho\overrightarrow{\vartheta}) + \nabla.\left(\rho\vec{\vartheta}\vec{\vartheta}\right) = -\nabla p + \nabla.\left[\mu\left(\nabla\vec{\vartheta} + \nabla\overrightarrow{\vartheta^T}\right)\right] + \rho\vec{g} + \vec{F} \tag{2}$$

where p is the static pressure, $\vec{\vartheta}$ is velocity, $\overrightarrow{\vartheta^T}$ is the stress tensor, $\vec{g}$ is the gravitational body force, ρ is the density of the fluid, μ is viscosity, and $\vec{F}$ is an external body force. The effect of gravity is negligible for pore-throat geometry in micrometres, hence, the density is kept the same for both fluids as the impact of density difference is small. The tracking of the interface(s) between the phases is accomplished by the solution of a continuity equation for the volume fraction of one (or more) of the phases. For the qth phase, it can be written as:

$$\frac{\partial\alpha_q}{\partial t} + \vec{\vartheta}\cdot\nabla\alpha_q = \frac{S\alpha_q}{\rho_q} \tag{3}$$

where $S\alpha_q$ is the source term representing the mass transfer between phases, that is taken as zero in our calculations. The volume fraction equation for the primary phase is computed using:

$$\sum_{q=1}^{n}\alpha_q = 1 \tag{4}$$

The presence of the component phases determines the properties appearing in the transport equations. The volume fraction averaged density is then computed as $\rho = \sum_{q=1}^{n}\alpha_q\rho_q$. Similarly, other properties can be obtained.

The phase interaction between the fluids can be defined in terms of the surface tension which is a force acting only at the surface and balances the radially inward intermolecular attractive force with the radially outward pressure gradient force across the surface. In regions where two fluids are separated, but one of them is not in the form of spherical bubbles, the surface tension acts to minimise free energy by decreasing the area of the interface. The continuum surface force (CSF) model is employed for the source term in the momentum equation. The pressure drop across the surface relies on the surface tension coefficient, σ, and the surface curvature as measured by two radii in orthogonal directions, R_p and R_q:

$$p_q - p_p = \sigma\left(\frac{1}{R_q} + \frac{1}{R_p}\right) \tag{5}$$

where p_q and p_p are the pressures in fluids q and p on either side of the interface. If n is the surface normal, then volume fraction of qth phase is $\nabla.\alpha_q$ and curvature k is given by $\nabla.\hat{n}$, where$\hat{n} = n/|n|$. The contact angle the fluid makes with a wall (θ_w) is used to adjust the surface normal in cells near the wall. If θ_w is the contact angle at the wall, then the surface normal at the cell next to the wall is:

$$\hat{n} = \hat{n}_w \cos\theta_w + \hat{t}_w \sin\theta_w \quad (6)$$

where $(\hat{n}_w)$ and $(\hat{t}_w)$ are the unit vectors normal and tangential to the wall. The curvature is also used to adjust the body force term in the surface tension calculation.

Case study and computational setup

We consider a simple geometry (Case 1) that contains one inlet and one outlet. This is consistent with the previous studies (Zhao and Wen 2017). However, this is much simpler than the actual case in rocks where triple junctions predominate. Hence, we conducted simulations on a system with a more realistic geometry, Case 2, which consists of one inlet and two outlets at 120° to each other. In both cases, we have selected a pore of 35 µm in diameter and a throat of 5 µm in diameter to be close to that found in oil-containing rocks. Both cases are schematically represented in Fig. 1.

A summary of the parameters used for simulations for both cases is given in Table 2. Different wettability values were simulated; 0° for water-wet, 90° for intermediate-wet and 180° for oil-wet states. This is motivated by the fact that the injection of nanoparticles alters the wettability, depending on nanoparticles concentration and properties. In addition to wettability, the injection of nanoparticles also changes IFT between oil and water. Hence, in this study, we considered different values of IFT as shown in Table 2. Both cases were studied for saturated and unsaturated oil conditions. For Cases 1.1–1.3 and 2.1–2.3, the pore-throat structure was initially saturated by oil where the volume fraction of oil is one whereas the volume

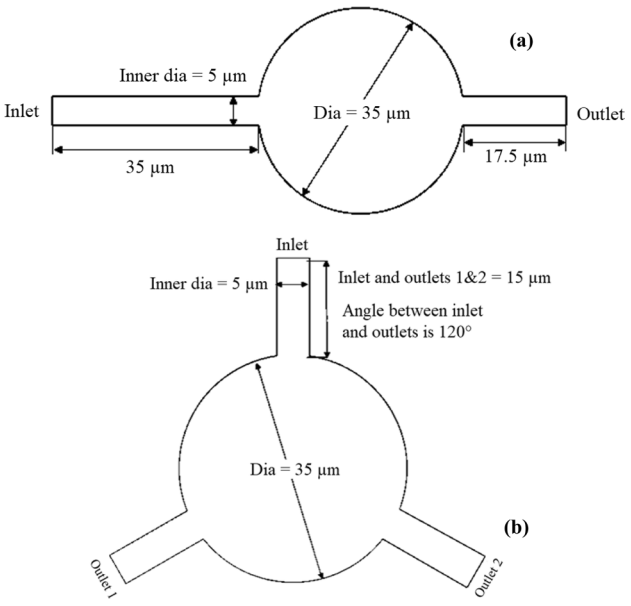

Fig. 1 **a** Case 1 and **b** Case 2 geometry

Table 2 Summary of cases

Cases	Partial oil drop diameter in the pore region (µm)	IFT (µN/m)	Contact angle (°)
Case 1.1	0	52E+3	0
Case 1.2	0	52E+3	90
Case 1.3	0	52E+3	180
Saturated oil condition			
Case 2.1	0	52E+3	0
Case 2.2	0	52E+3	90
Case 2.3	0	52E+3	180
Unsaturated oil condition			
Case 1.4	15	52	180
Case 1.5	9	52	180
Case 2.4	15	52	180
Case 2.5	9	52	180
Case 2.6	9	10	180
Case 2.7	9	35	180
Case 2.8	9	65	180
Case 2.9	9	75	180

fraction of water is 0. The IFT was set to 52×10^3 µN/m and contact angles were 0° (cases 1.1 and 2.1), 90° (cases 1.2 and 2.2) and 180° (cases 1.3 and 2.3). For cases 1.4, 1.5 (two droplets) and 2.4–2.9 (three droplets) representing the unsaturated oil conditions, two different oil droplet sizes of 9 µm and 15 µm are considered. The IFT value for Cases 1.4, 1.5, 2.4 and 2.5 was 52 µN/m whereas for cases 2.6–2.9, it ranges 10–75 µN/m. For the unsaturated oil conditions, the contact angle was 180°. The density of both dormant fluid (oil) and injected fluid (water) was set at 1000 kg/m^3. However, the fluids are differentiated by their viscosities which for water was set at 0.001 Pa.s and for oil was set at 0.01 Pa.s ($\frac{\mu_w}{\mu_o} = 10$). The domain is initialised by a constant velocity of 0.005 m/s and ambient pressure in all cases.

The simulations were conducted using Ansys/Fluent. The coupled pressure–velocity scheme was adopted. A Courant number value of 0.75 was used to stabilise the convergence behaviour, resulting in computational times between 1×10^{-9} s and 1×10^{-6} s. The residuals were smaller than 1×10^{-4} for all variables. The velocity inlet boundary condition was set at the inlet, imposing a gauge pressure of zero at the inlet. The water is injected with a constant velocity of 0.005 m/s in the direction normal to the boundary. The pressure outlet boundary condition was implemented at the outlets. The total pressure was considered for backflow specification with a temperature of 300 K where the backflow direction is normal to the boundary. It applies the combined effects of gauge pressure and dynamic velocity contribution based on the

velocity in the adjacent cell zone. The continuum surface force model is used in the presence of wall adhesion, allowing the modelling of the surface tension force.

Results and discussion

Grid independency

The Multizone Quad/Tri method was used to generate a structured mesh. To ensure the results are not affected by the mesh resolution, a mesh independence study was first conducted for Case 1.2 where the contact angle and the surface tension are 90° and $52 \times 10^{+3}$ µN/m, respectively. Following Zhao and Wen (2017), we considered the static pressure for the grid independency at the point near Inlet. We also monitored velocity, however, since the velocity magnitude at the inlet is very small (0.005 m/s), it does not show significant change. Therefore, static pressure is shown here. Three different mesh resolutions were tested; 0.25 µm, 0.35 µm, and 0.5 µm, which resulted in 19,600, 9225 and 7652 computational cells. Figure 2 presents the static pressure profile along the X-direction at location $P_{1,}$ which is 40 µm from the centre of the pore towards the inlet. Results were obtained for three different mesh sizes at 3 ms flow time. The static pressure profile was initially sensitive to the mesh resolution while a reduction in the mesh size from 0.35 to 0.25 µm marginally affected the pressure distribution, confirming that a 0.35 µm mesh resolution is suitable. A closeup snapshot of the selected mesh in the pore region is shown in Fig. 3. A similar mesh resolution is applied for the second geometric configuration.

Nanofluid flooding

Two parameters are computed using the CFD data for different contact angles and surface tensions; the ORF and the

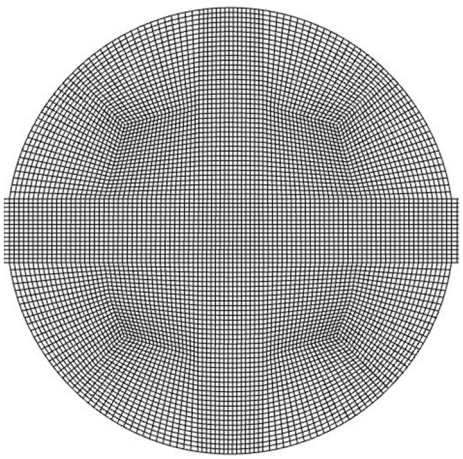

Fig. 3 A mesh snapshot for the pore region

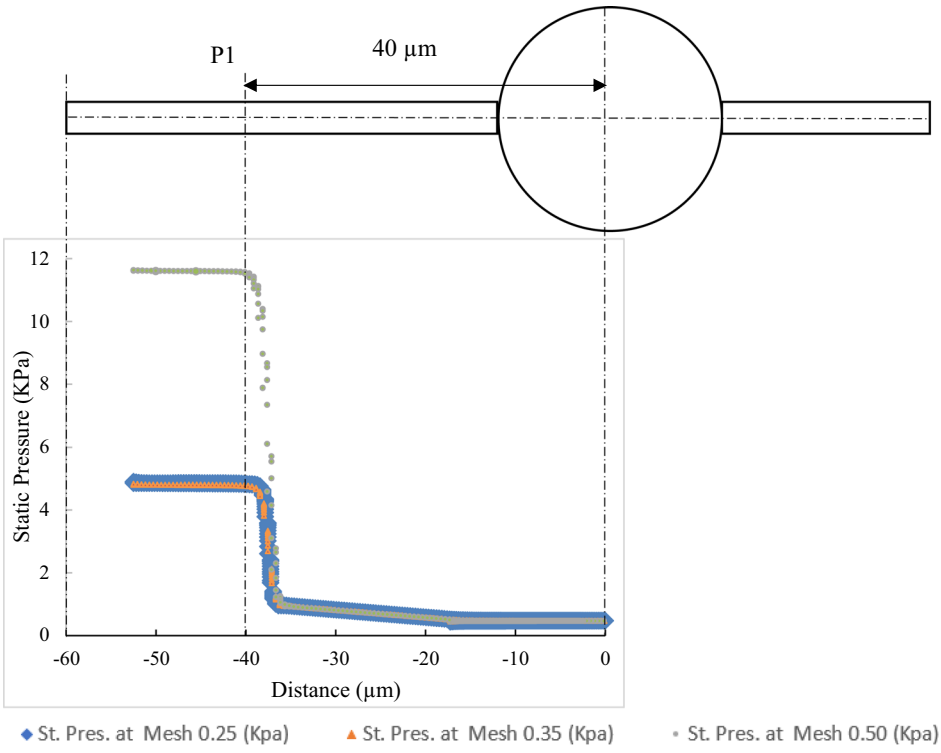

Fig. 2 Static pressure at 3 ms flow time

flow time. The ORF is calculated using the volume-weighted average of volume fraction for the entire domain using

$$\alpha = \frac{1}{V}\int \alpha dV = \frac{1}{V}\sum_{q=1}^{n} \alpha_q |V_q| \tag{7}$$

where α_q is volume fraction at cell q and V_q is the cell volume. The oil recovery is then computed. The given flow time is referred to as the physical time when the maximum ORF is achieved in each case.

Saturated oil condition

Three conditions were numerically analysed to study flow characteristics and the oil recovery factor at a contact angle of 0° (water-wet state), 90° (intermediate state), and 180°

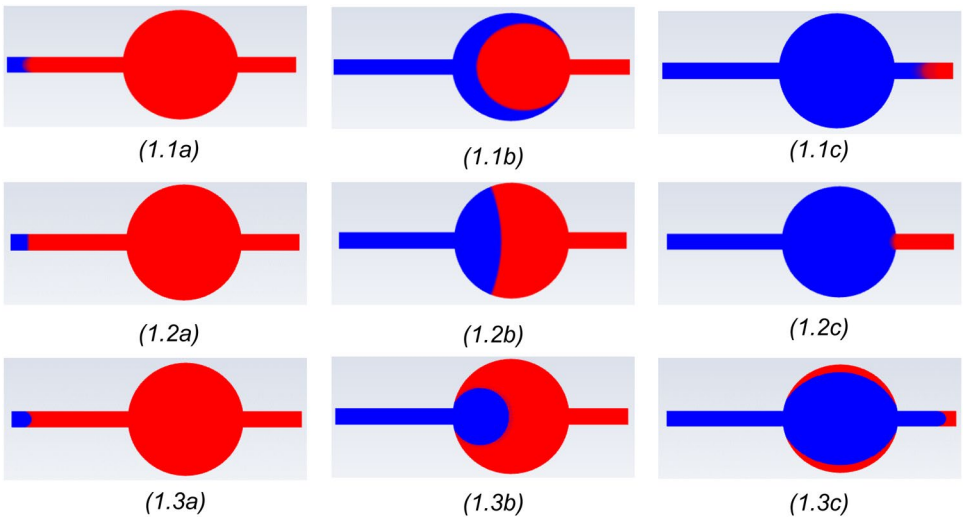

Fig. 4 Volume fraction of cases at (1.1) Water-wet, (1.2) Intermediate-wet and (1.3) Oil-wet states at different flow times **a** 1 ms; **b** 20 ms; and **c** 45 ms

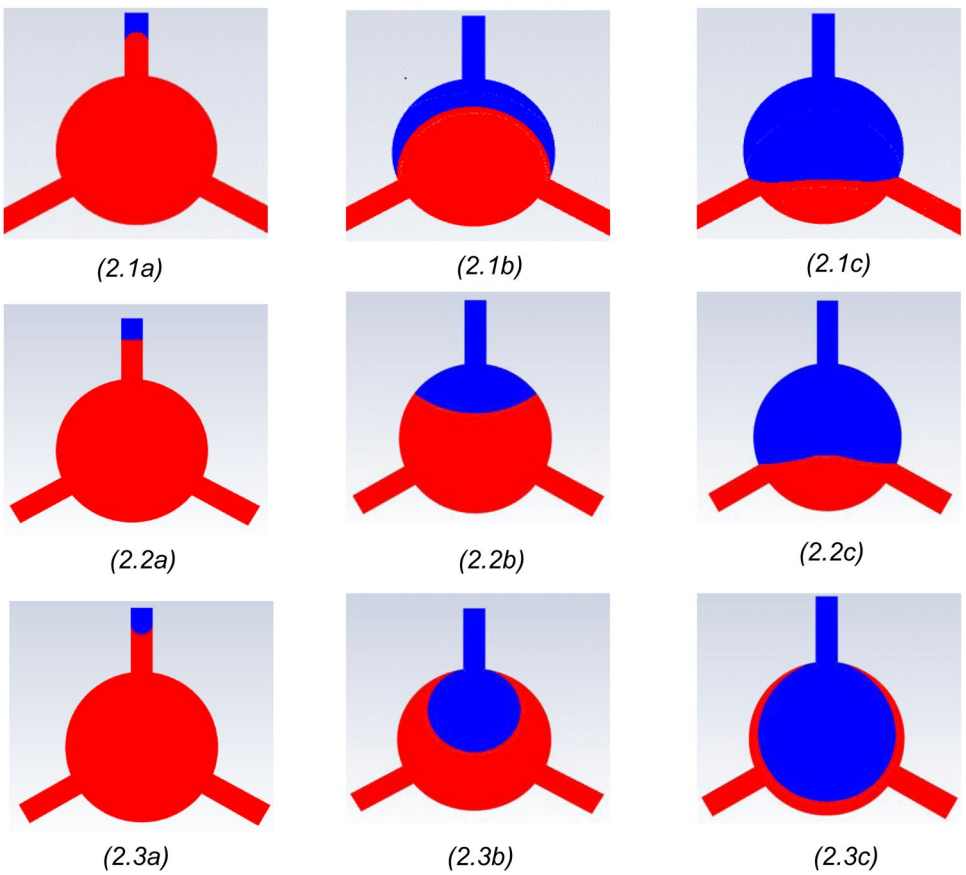

Fig. 5 Volume fraction of cases at (2.1) Water-wet, (2.2) Intermediate-wet and (2.3) Oil-wet state at different flow times **a** 1 ms; **b** 12 ms; and **c** 30 ms

(oil-wet state). The time series of volume fraction development are shown in Figs. 4 and 5 for Case 1 and Case 2 at the water-wet, intermediate-wet and oil-wet states. The profiles for the water-wet state show that the oil–water interface is concave and that it retains that shape until the oil is fully recovered. In all figures representing the volume fraction contour plots, oil is shown in red and water is shown in blue. To the best of our knowledge, there are no experimental studies on such a configuration that can be used for the validation, however, for simple geometry (Cases 1.1, 1.2 and 1.3 in Fig. 4), the obtained results qualitatively follow the trend observed in the previous studies (Zhao and Wen 2017) for a similar pore structure although they are not identical. It can be seen that as the contact angle changes from 0° to 180°, wettability changes which affected the oil recovery. At 0° contact angle, 99% oil recovery was achieved but at 180° only 87% oil recovery was accomplished. This is consistent with the results presented by (Zhao and Wen 2017), confirming the accuracy of the simulations.

Although Case 1.1 results in 99% oil recovery, in Case 2.1, oil recovery does not exceed 60.0%. This is due to the reverse flow occurring at 28 ms. To eliminate this unphysical response, the length of the outlet pipes was increased to 40 µm, resulting in an ORF of 99% for Case 2.

The volume fractions for the intermediate state where the contact angle is 90° differ from the water-wet state since the intermediate-water interface remains straight until injected water reaches the outlet where it curved slightly towards the exit outlet. For the intermediate state, Case 1.2 and Case 2.2 recovered approximately 99%. As shown in Figs. 1.2b and 2.2b, the flow tends to balance which is shown by a slight curve because the contact angle is 90°. For the oil-wet state (Figs. 4 (1.3) and 5 (2.3)), in both geometric models, the oil–water interface shows a convex profile towards the outlet leaving behind some amount of oil near the pore walls showing that viscosity of the oil is higher than water. At the oil-wet state, Case 1.3 recovered 87.72%, and Case 2.3 recovered 89.66% of oil. The incoming fluid changes the case from oil-wet to water-wet but some oil is trapped at the walls of the pore. The ORF values for Case 1.3 and Case 2.3 are close with only a difference of 2%, confirming that both geometries are following the same trends with marginal differences in ORF.

The wettability differs from the oil-wet state to the intermediate-wet and finally to a water-wet state. It can be concluded that after primary oil recovery, some of the oil remains stuck to the walls of the pore for both Case 1 and Case 2. The water-wet state can recover the maximum amount of oil by altering wettability which can be achieved by, for example, introducing nanoparticles to the medium. The volume fraction profiles represent the wettability—the oil–water interface changes with the state of the system. In the water-wet state where the contact angle is 0°, there

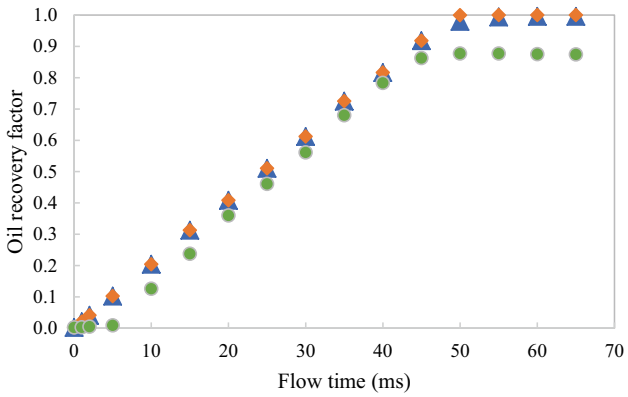

Fig. 6 Oil recovery factors Cases 1.1 (blue triangle), 1.2 (orange diamond) and 1.3 (green circle)

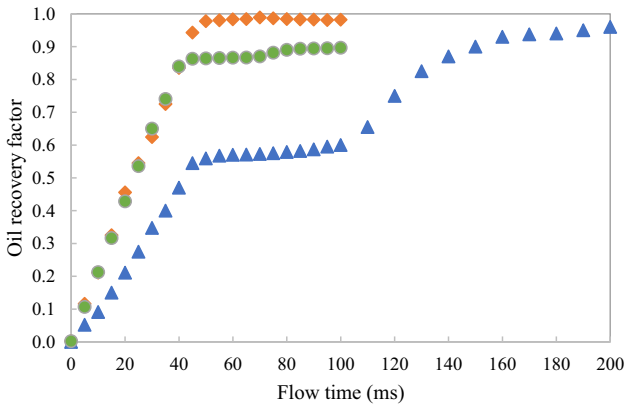

Fig. 7 Oil recovery factors Cases 2.1 (blue triangle), 2.2 (orange diamond) and 2.3 (green circle)

are maximum cohesive forces and profile shape is concave. At the intermediate state, when the contact angle is 90°, both fluids are balanced/neutral, and therefore the profile is straight. Meanwhile, at the oil-wet state, both fluids have minimum cohesion for a contact angle of 180°, and hence the oil–water interface has a convex profile.

The temporal evolution of the ORF as a function of the flow time is shown in Figs. 6 and 7 for Case 1 and Case 2, respectively. Although it was observed that the steady-state ORF marginally changes as the pore structure varies, there is a significant difference in time-dependent ORF trend. Case 1 is a simple pore-throat section with negligible gravity, achieving the maximum ORF at 66, 48 and 49.5 ms for contact angles of 0° (Case 1.1), 90° (Case 1.2), and 180° (Case 1.3), respectively. On the other hand, the second geometric configuration comprises an inlet and two inclined outlets at 120° with zero gravitational force. The maximum oil recovery for the contact angles of 90° (Case 2.2) and 180° (Case 2.3) occur at 70 and 100 ms, respectively whereas the

contact angle of 0° (Case 2.1) requires 200 ms to recover 99% of the oil. The geometric configuration can justify this since the contact angle of 180° has the least cohesive forces; therefore, the behaviour of oil is the same for Case 2.3 and Case 1.3. A contact angle of 90° is equivalent to no wall adhesion effects where the interface is normal to the adjacent wall for both oil and water fluids. Therefore, the maximum oil recovery of 99% was achieved for Case 1.2 and Case 2.2. At a contact angle of 0°, maximum cohesive forces acted on the fluid and the wall, in the presence of low inlet velocity. It is worth noting that the outlet was extended in Case 2.1 to avoid the occurrence of reverse flow. However, the temporal evolution of ORF is computed for the same region as Case 2.2. Saturated oil simulations show that in Case 1, 12% more oil is recovered in the water-wet state compared to the oil-wet state, while this is 10% for Case 2.

The time for the maximum ORF for the saturated oil state is given in Fig. 8 for both geometric models. We see that Case 2.1 at the water-wet state achieves the maximum ORF at a longer time than Case 1.1. This is due to the modification of the geometry in Case 2. The results show that the second geometric model, being more complex, has a longer breakthrough time for all three conditions. It can be seen that Case 2 shows a different trend as the contact angle varies.

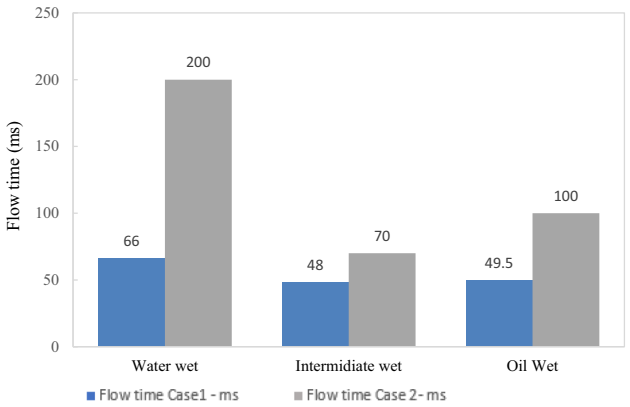

Fig. 8 Flow time to achieve maximum ORF for saturated oil condition

While Case 1 shows a marginal difference in the flow time for intermediate and oil-wet states, Case 2 results in 40% longer flow time for the oil-wet state compared to the intermediate state. The ORF ratios between Cases 1 and 2 at water-wet, intermediate- and oil-wet states are 3.0, 1.46 and 2.0, respectively.

Unsaturated oil condition

For the initial oil-wet state with the same injecting velocity of the invading fluid, the flooding process was studied for the unsaturated oil condition. Two situations were considered: the first scenario contains partial oil drops with a diameter of 9 µm and the second scenario includes partial oil droplets with a diameter of 15 µm. Case 1 includes two partial oil drops while Case 2 contains three partial oil drops. The initial oil volume fraction in the pore region varies between 12 and 62%. The IFT for the unsaturated condition is set much smaller than the saturated condition since the nanofluid invasion is assumed, which resulted in an ultra-low IFT state. Thus, considering wettability from oil-wet state to water-wet state along with low IFT value defends the combined wettability and IFT effect on the pore-scale geometry. The time series of volume fraction distributions for Cases 1.4, 1.5, 2.4 and 2.5 are presented in Figs. 9 and 10, showing the combined effect of both wettability and IFT. The 180° contact angle was considered as oil-wet state with reduced IFT value of 52 µN/m. During the early stage of flooding, some oil remains stuck to the pore walls that is represented in a droplet shape. Cases 1.4 and 1.5 recover 99% of the oil in 250 and 435 ms, respectively, showing that smaller oil particles take more time to be recovered. For Case 2.4, 99% oil recovery was obtained at 170 ms whereas for Case 2.5 a maximum oil recovery of 68% was achieved. It can be concluded that even in the presence of a very low IFT nanofluid, recovery of small oil drops is extremely slow. Also, for the complex geometric configuration, a longer duration is required for maximum oil recoveries. The behaviour of the oil droplets in these cases shows that the oil-wet state gradually changes as the oil drops are detached from the walls and progressively move towards the outlet, confirming

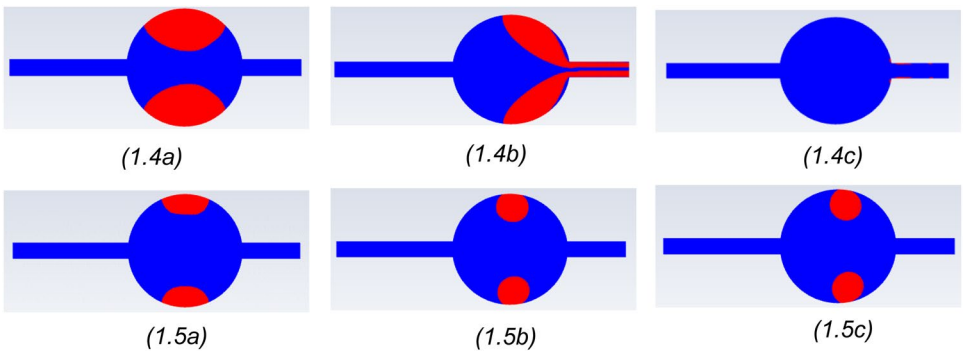

Fig. 9 Volume fraction of the wettability and IFT combined effect on Case 1 unsaturated oil state (2-droplets (1.4) 15 µm dia and (1.5) 9 µm dia.) at different flow times **a** 1 ms; **b** 25 ms; and **c** 70 ms

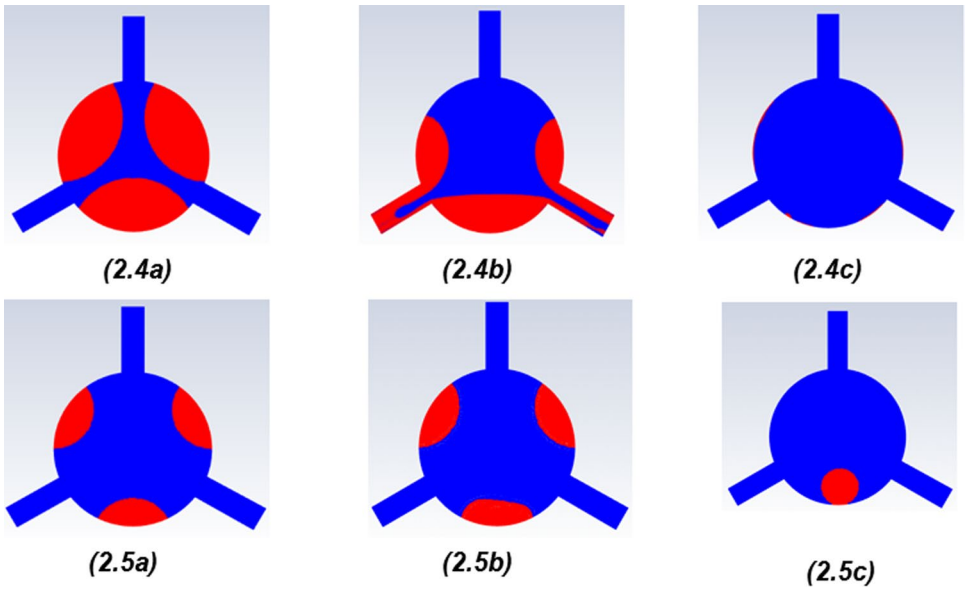

Fig. 10 Volume fraction of the wettability and IFT combined effect on Case 2 unsaturated oil state (3-droplets (2.4) 15 µm dia and (2.5) 9 µm dia.; surface tension 52 µN/m) at different flow times **a** 0.1 ms; **b** 20 ms; and **c** 120 ms

smaller oil droplets consume more time for detachment and achieving 99% ORF.

Figure 11 illustrates the unsaturated oil situation for Case 1 and Case 2 with an IFT of 52 µN/m at 200 ms flow time. It shows that 99% of ORF is achieved at 75 ms and 200 ms for Case 1.4 (15 µm partial oil drops) and Case 1.5 (9 µm partial oil drops), respectively. Case 2.4 reaches 99% at 200 ms but case 2.5 only reached 68% at the same time and it then remains constant. It showed that the recovery is not only affected by complex geometry but also the size of oil droplet is important. The smaller the droplet size, the more time is consumed to achieve maximum recovery.

To further analyse the effect of IFT at unsaturated conditions, IFT values of 10 µN/m (Case 2.6), 35 µN/m (Case 2.7), 65 µN/m (Case 2.8) and 75 µN/m (Case 2.9) were used with the second geometric model. A contact angle of 180° and partial oil drops of 9 µm diameter (15% oil) were used. Figure 12 shows the volume fraction at 0.1 ms, 50 ms and 100 ms for Case 2.6 to Case 2.9. The trend shows that initially at 0.1 ms, the ORF is zero. At 50 ms, the trapped oil droplets start moving although the oil recovery is still zero. At 100 ms, the ORF was still zero but left and right side droplets started moving towards left and right outlets, respectively, confirming the importance of IFT on the time-dependent ORF. Here, the geometric configuration is in micrometres, representing the rock configures where small oil droplets are trapped. The introduction of nanoparticles changes the viscosity and interfacial tension of the mixture

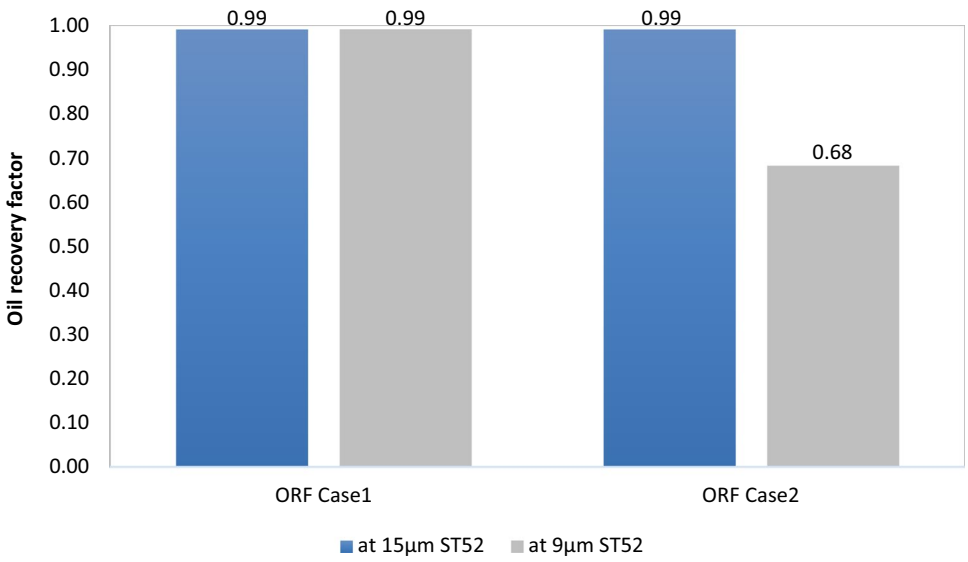

Fig. 11 Oil recovery factors for unsaturated oil condition at 200 ms for Case 1 and Case 2

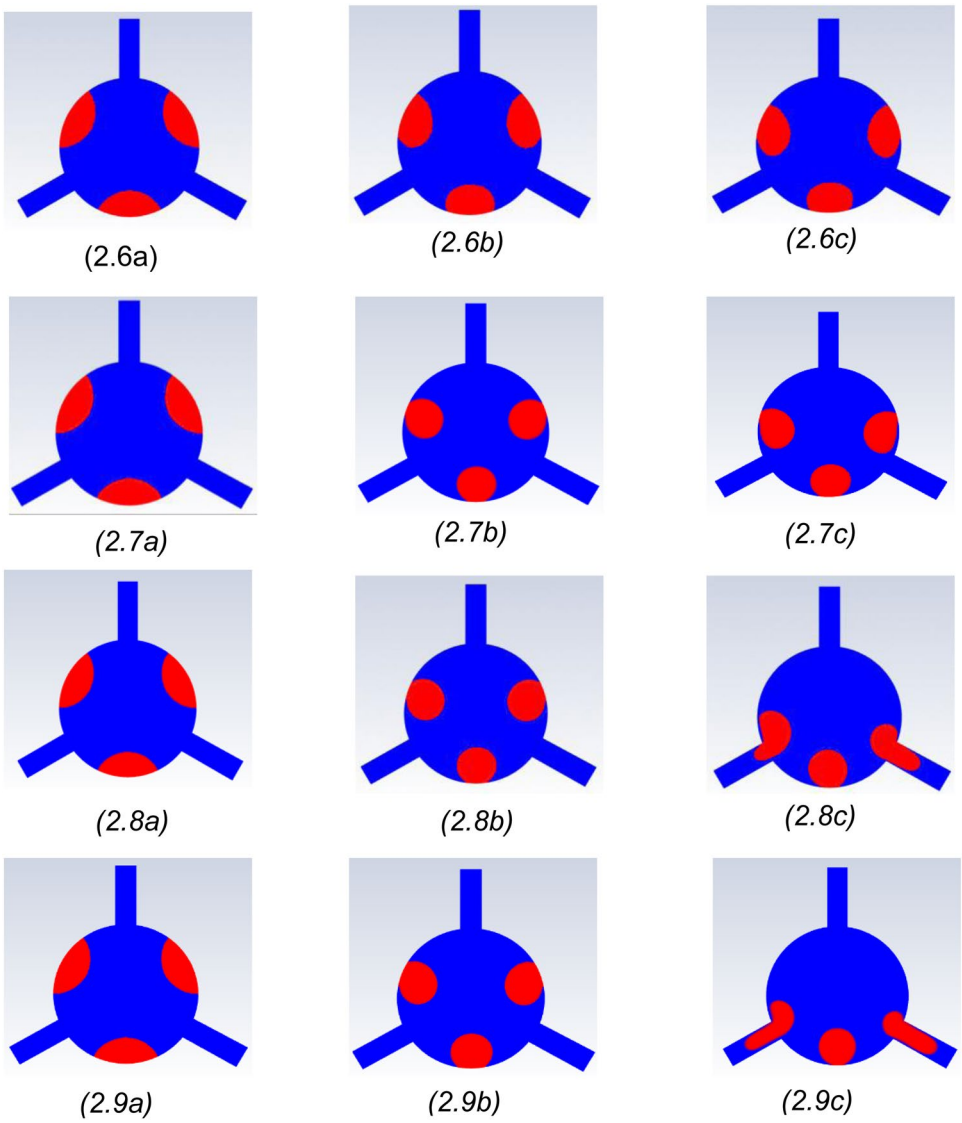

Fig. 12 Volume fraction of the wettability and IFT combined effect on Case 2 unsaturated oil state (3-droplets 9 µm dia.) surface tension (2.6) 10 µN/m (2.7) 35 µN/m (2.8) 65 µN/m and (2.9) 75 µN/m at different flow times (**a**) 0.1 ms; (**b**) 50 ms; and (**c**) 100 ms

that assists to extract the oil droplets trapped in the pore towards the outlet although the process is slow. There are some suggestions to overcome this issue. Increasing the inlet velocity may speed up the process, however, it is important the flow remains laminar since turbulent flows may tend to damage the walls of the reservoir and may cause failure (Youssif et al. 2018). Alternately, increasing the concentration of nanoparticles may enhance the process, however, they may enter the wall structure and react with the rock, dragging rock particles along with the oil which will have an overall negative impact on the oil recovery, resulting in failure of reservoir structure. These could be further investigated in future work.

Figure 13 shows the time variation of ORF for Case 2, with 15% initial oil and a range of IFT values. It can be seen that at 100–120 ms, all cases except Case 2.6 (10 µN/m) achieved the maximum oil recovery of 68%. For Case 2.6, the maximum oil recovery of 68% was achieved at 240 ms. This process is time-consuming because the microscopic oil droplets that are stuck to the walls of the rocks need more time to change their wettability, detach and move through the injected fluid towards the outlet. This finding is in agreement with previous studies (Zhao and Wen 2017). Lv and Wang (2015) also stated that the oil-wet state contact angle and oil saturation could significantly affect displacement behaviour and ORF. Gharibshahi et al. (2015) concluded that injection of nanofluids improves the ORF, considerably. The sudden change of oil recovery from zero to its maximum is because the oil droplets at the left and right simultaneously moved toward the outlet whereas the initial droplet at the bottom remains unchanged in the simulation time considered here.

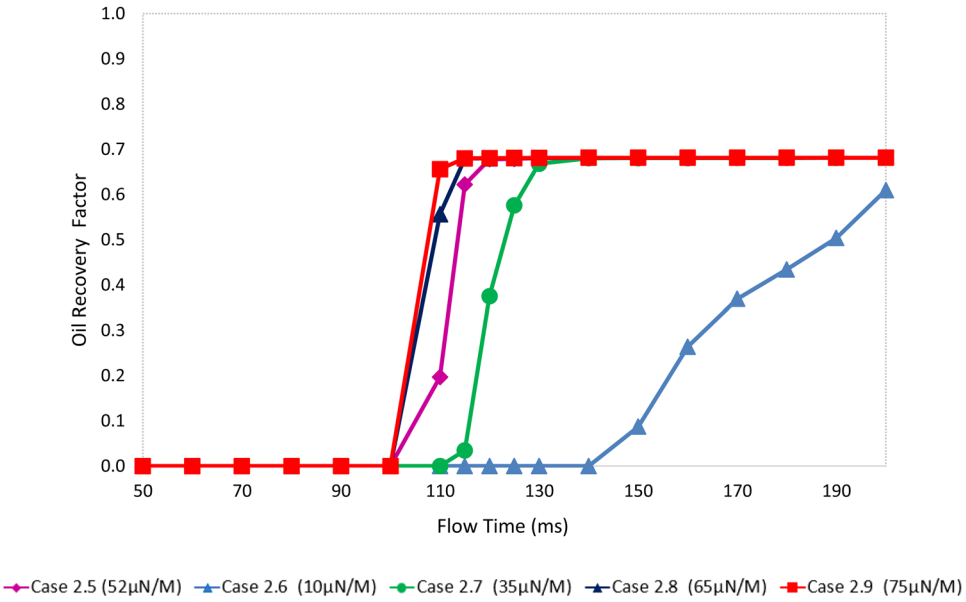

Fig. 13 Oil recovery factors (unsaturated oil condition) Case 2–9 µm oil drops at different surface tensions

Conclusion

A comprehensive set of computational fluid dynamic (CFD) simulations were conducted for two geometries: a single pore with one inlet and one outlet (Case 1) and a single pore with one inlet and two outlets (Case 2). The CFD model applied the Volume of Fluid method to the pore-scale models considered in this study. The effects of wettability, contact angle, and interfacial tension (IFT) were studied on these two geometric micromodels for saturated and unsaturated oil conditions. The main findings can be summarised as follows:

- At oil-saturated state, both the simplified pore-throat model (Case 1) and the more realistic pore structure (Case 2) achieved 99% ORF. For Intermediate-wet state, both Cases 1 and 2 achieved 99% oil recovery. In the oil-wet state, partial recoveries of 87.7% and 89.6% occurred for Case 1 and Case 2, respectively.
- There were significant differences in the trends of time-dependent oil recovery factor between Case 1 and Case 2. For the more complex geometry, longer times (about 1.4 to 3 times more) were required to achieve maximum oil recovery compared to the simplified configuration.
- A similar trend was observed for the unsaturated oil state. Both cases achieved 99% oil recovery while the required time was significantly higher for Case 2. Case 1 with 15 µm initial partial oil drops attained 99% oil recovery at 75 ms, while Case 1 with 9 µm initial partial oil drops resulted in 99% oil recovery in 220 ms. The required time for oil recovery is significantly higher in Case 2. The results showed that for larger oil droplets, it took 170 ms for 99% of oil recovery which is approximately 2.3 times more than Case 1 with similar initial oil volume in the pore region. For smaller droplets, a maximum oil recovery of 68% was achieved in the complex geometry (Case 2). Thus, it was confirmed that the impact of pore structure becomes more significant in the unsaturated oil state.
- Case 2 was further studied for different IFT values, demonstrating the oil recovery became slower at very low IFT values.

This study shows that the pore structure significantly affects the temporal behaviour of the oil recovery, confirming a realistic case study is vital to understand the oil recovery mechanism in complex practical applications. Future studies are required for 3D analysis of pore structure using both experimental and numerical techniques while the complexity of the geometry is systematically increased. Well-characterised experimental studies of such flows will particularly provide detailed measurement data for the model validation. It is also important to understand the effects of different parameters in the presence of surfactant on oil recovery factors as well as pressure and temperature distributions.

Acknowledgements This work is benefited from computational resources on the Australian National Computational Infrastructure.

Funding Not application.

Declarations

Conflict of interest On behalf of all authors, the corresponding author states that there is no conflict of interest.

References

Arif M, Al-Yaseri AZ, Barifcani A, Lebedev M, Iglauer S (2016) Impact of pressure and temperature on CO_2-brine-mica contact angles and CO_2-brine interfacial tension: Implications for carbon geo-sequestration. J Colloid Interface Sci 462:208–215. https://doi.org/10.1016/j.jcis.2015.09.076

Chinnam J, Das D, Vajjha R, Satti J (2015) Measurements of the contact angle of nanofluids and development of a new correlation. Int Commun Heat Mass Transf 62:1–12. https://doi.org/10.1016/j.icheatmasstransfer.2014.12.009

Gharibshahi R, Jafari A, Haghtalab A, Karambeigi MS (2015) Application of CFD to evaluate the pore morphology effect on nanofluid flooding for enhanced oil recovery. RSC Adv 5:28938–28949. https://doi.org/10.1039/c4ra15452e

Hashemi SI, Fazelabdolabadi B, Moradi S, Rashidi AM, Shahrabadi A, Bagherzadeh H (2016) On the application of NiO nanoparticles to mitigate in situ asphaltene deposition in carbonate porous matrix. Appl Nanosci 6:71–81. https://doi.org/10.1007/s13204-015-0410-1

Hendraningrat L, Torsæter O (2015) Metal oxide-based nanoparticles: revealing their potential to enhance oil recovery in different wettability systems. Appl Nanosci. https://doi.org/10.1007/s13204-014-0305-6

Hendraningrat L, Zhang J (2015) Polymeric nanospheres as a displacement fluid in enhanced oil recovery. Appl Nanosci 5:1009–1016. https://doi.org/10.1007/s13204-014-0399-x

Iglauer S, Mathew MS, Bresme F (2012) Molecular dynamics computations of brine-CO_2 interfacial tensions and brine-CO_2-quartz contact angles and their effects on structural and residual trapping mechanisms in carbon geo-sequestration. J Colloid Interface Sci 386:405–414. https://doi.org/10.1016/j.jcis.2012.06.052

Jafari A, Pour SEF, Gharibshahi R (2017) CFD simulation of biosurfactant flooding into a micromodel for enhancing the oil recovery. Int J Chem Eng Appl 7:353–358. https://doi.org/10.18178/ijcea.2016.7.6.604

Joonaki E, Ghanaatian S (2014) The application of nanofluids for enhanced oil recovery: effects on interfacial tension and coreflooding process. Pet Sci Technol 32:2599–2607. https://doi.org/10.1080/10916466.2013.855228

Khalili Nezhad SS, Cheraghian G (2016) Mechanisms behind injecting the combination of nano-clay particles and polymer solution for enhanced oil recovery. Appl Nanosci 6:923–931. https://doi.org/10.1007/s13204-015-0500-0

Kim SJ, Bang IC, Buongiorno J, Hu LW (2006) Effects of nanoparticle deposition on surface wettability influencing boiling heat transfer in nanofluids. Appl Phys Lett. https://doi.org/10.1063/1.2360892

Kondiparty K, Nikolov A, Wu S, Wasan D (2011) Wetting and spreading of nanofluids on solid surfaces driven by the structural disjoining pressure: statics analysis and experiments. Langmuir 27:3324–3335. https://doi.org/10.1021/la104204b

Liu MS, Lin MCC, Wang CC (2011) Enhancements of thermal conductivities with cu, CuO, and carbon nanotube nanofluids and application of MWNT/water nanofluid on a water chiller system. Nanoscale Res Lett 6:297. https://doi.org/10.1186/1556-276X-6-297

Lv M, Wang S (2015) Pore-scale modeling of a water/oil two-phase flow in hot water flooding for enhanced oil recovery. RSC Adv 5:85373–85382. https://doi.org/10.1039/c5ra12136a

Nandwani SK, Chakraborty M, Gupta S (2019) Chemical flooding with ionic liquid and nonionic surfactant mixture in artificially prepared carbonate cores: a diffusion controlled CFD simulation. J Pet Sci Eng 173:835–843. https://doi.org/10.1016/j.petrol.2018.10.083

Radiom M, Yang C, Chan WK (2009) Characterization of surface tension and contact angle of nanofluids. Fourth Int Conf Exp Mech 7522:75221D. https://doi.org/10.1117/12.851278

Rostami P, Sharifi M, Aminshahidy B, Fahimpour J (2019) The effect of nanoparticles on wettability alteration for enhanced oil recovery: micromodel experimental studies and CFD simulation. Pet Sci 16:859–873. https://doi.org/10.1007/s12182-019-0312-z

Santiago C, Ghomeshi S, Kryuchkov S, Kantzas A (2016) Pore level modeling of imbibition in heavy oil saturated media. J Pet Sci Eng 140:108–118. https://doi.org/10.1016/j.petrol.2016.01.012

Saraji S, Piri M, Goual L (2014) The effects of SO_2 contamination, brine salinity, pressure, and temperature on dynamic contact angles and interfacial tension of supercritical CO_2/brine/quartz systems. Int J Greenh Gas Control 28:147–155. https://doi.org/10.1016/j.ijggc.2014.06.024

Sefiane K, Skilling J, MacGillivray J (2008) Contact line motion and dynamic wetting of nanofluid solutions. Adv Colloid Interface Sci 138:101–120. https://doi.org/10.1016/j.cis.2007.12.003

Vafaei S, Wen D, Borca-Tasciuc T (2011) Nanofluid surface wettability through asymptotic contact angle. Langmuir 27:2211–2218. https://doi.org/10.1021/la104254a

Wasan DT, Nikolov AD (2003) Spreading of nanofluids on solids. Nature 423:156–159. https://doi.org/10.1038/nature01591

Youssif MI, El-Maghraby RM, Saleh SM, Elgibaly A (2018) Silica nanofluid flooding for enhanced oil recovery in sandstone rocks. Egypt J Pet 27:105–110. https://doi.org/10.1016/J.EJPE.2017.01.006

Zhao J, Wen D (2017) Pore-scale simulation of wettability and interfacial tension effects on flooding process for enhanced oil recovery. RSC Adv 7:41391–41398. https://doi.org/10.1039/c7ra07325a